# Recent Advances in Defect-Engineered Transition Metal Dichalcogenides for Enhanced Electrocatalytic Hydrogen Evolution: Perfecting Imperfections

Zheng Hao Tan, Xin Ying Kong,* Boon-Junn Ng, Han Sen Soo, Abdul Rahman Mohamed, and Siang-Piao Chai*

Read Online

ACCESS | Metrics & More | Article Recommendations

**ABSTRACT:** Switching to renewable, carbon-neutral sources of energy is urgent and critical for climate change mitigation. Despite how hydrogen production by electrolyzing water can enable renewable energy storage, current technologies unfortunately require rare and expensive platinum group metal electrocatalysts, which limit their economic viability. Transition metal dichalcogenides (TMDs) are low-cost, earth-abundant materials that possess the potential to replace platinum as the hydrogen evolution catalyst for water electrolysis, but so far, pristine TMDs are plagued by poor catalytic performances. Defect engineering is an attractive approach to enhance the catalytic efficiency of TMDs and is not subjected to the limitations of other approaches like phase engineering and surface structure engineering. In this minireview, we discuss the recent progress made in defect-engineered TMDs as efficient, robust, and low-cost catalysts for water splitting. The roles of chalcogen atomic defects in engineering TMDs for improvements to the hydrogen evolution reaction (HER) are summarized. Finally, we highlight our perspectives on the challenges and opportunities of defect engineering in TMDs for electrocatalytic water splitting. We hope to provide inspirations for designing the state-of-the-art catalysts for future breakthroughs in the electrocatalytic HER.
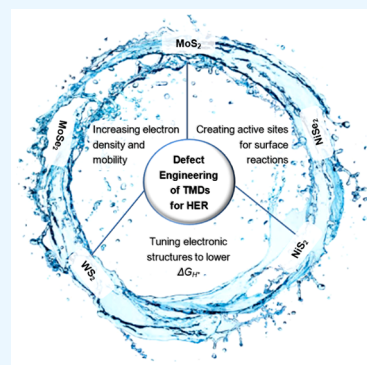
## 1.0. INTRODUCTION

Climate change caused by anthropogenic carbon dioxide ($CO_2$) emissions poses an existential threat to humanity.[1] Achieving net zero carbon emissions by 2050 to keep the global average temperature rise to below 2 °C above preindustrial times is necessary to avoid the disastrous effects of global warming, which can include more extreme weather events and rising sea levels.[2] A key aspect of climate change mitigation is to reduce $CO_2$ emissions by switching from fossil fuel combustion to the use of renewable energy sources including solar and wind energy.[3] Nevertheless, renewable energy sources are intermittent in nature, meaning that storage of the renewably produced electricity is essential to meet humanity's energy demands.[4] Among the existing approaches, electrochemically synthesizing chemical fuels is one of the most promising and sustainable ways to store renewable energy by converting the ubiquitous substances such as water, nitrogen, and $CO_2$ into value-added fuels including hydrogen,[5] ammonia,[6] and formate,[7] respectively. Specifically, hydrogen is an excellent fuel since it possesses a high energy density of 142 MJ/kg and is versatile use because it can be converted back into electricity in a fuel cell or can be mixed with natural gas and combusted for municipal cooking and heating.[8] More importantly, hydrogen produces only the environmentally benign water when it is oxidized to release its stored energy.[9,10]

Currently, hydrogen is conventionally produced by steam-methane reforming (gray hydrogen), which is an energy-intensive process that produces $CO_2$ as a byproduct. Although the released $CO_2$ can be captured and sequestered to mitigate the global warming impact, the production of hydrogen by electrolyzing water using renewable electricity (green hydrogen) would be more desirable and environmentally sustainable because it will not involve any fossil fuel, namely methane, or produce $CO_2$ in the first place.[11] However, hydrogen production by water electrolysis requires effective electrocatalysts to achieve a high energy conversion efficiency. Presently, the best-performing catalysts employed in commercial water electrolyzers are platinum-group metals (PGMs), such as platinum (Pt), rhodium (Rh), palladium (Pd), and iridium (Ir).[12] However, these PGMs are noble metals that are rare and expensive, and mining these metals causes negative environmental impacts, making the use of PGMs for large-scale

commercial water electrolysis both economically unviable and environmentally unsustainable.[11,13−15] Transition metal dichalcogenides (TMDs) refer to a group of compounds with the chemical formula of $MX_2$, where $M$ corresponds to a transition metal (group 4−10) such as molybdenum (Mo, group 6), tungsten (W, group 6), or nickel (Ni, group 10), whereas $X$ is a chalcogen (group 16) such as sulfur (S) or selenium (Se).[16] In 2005, the pioneering work published by Hinnemann et al. suggested that $MoS_2$ can theoretically exhibit catalytic activity comparable to Pt for the hydrogen evolution reaction (HER).[17] Since then, a myriad of TMD materials have been studied extensively as HER catalysts, with the goal of replacing Pt by a more abundant and cheaper alternative. Particularly, group 4−7 TMDs, such as molybdenum disulfide ($MoS_2$), molybdenum diselenide ($MoSe_2$), and tungsten disulfide ($WS_2$) have received paramount research attention. Being a two-dimensional (2D) material with a layered structure similar to graphene, the bulk crystalline structure of TMDs is made up of stacked layers, which is analogous to graphite being made up of graphene layers.[16] Unfortunately, the basal plane of pristine 2D TMDs is proposed to be catalytically inert, which handicaps the overall HER electrocatalytic performance.[18]

Over the years, various strategies such as phase, surface structure, and defect engineering have been explored to increase the exposure of the catalytically active sites and activate the basal planes of TMDs for improved catalytic activities. Among these approaches, defect engineering of TMDs by artificially inducing chalcogen or metal vacancies has attracted enormous research attention in the recent years. The presence of vacancies breaks the lattice periodicity and alters the lattice arrangements of the TMDs, leading to the tuning of electronic structures. Other than inducing the surface active sites and activating the basal planes of TMDs, the opportune concentration of vacancies on the basal planes of TMDs can regulate the dynamic processes of electrons transfer and local ions diffusion, which are highly beneficial for electrocatalytic HER.[19] Rather than provide an exhaustive discussion of all the strategies for improving the HER performance of TMDs, this minireview mainly outlines the defect engineering of TMDs with reference to the publications in recent years. We start with a brief discussion about the foundational knowledge of electrocatalytic HER to give an overview of the field to readers who are new to this area. Subsequently, the approaches to artificially induce defects in TMDs and the pivotal roles of defects for enhanced HER activity are discussed, focusing on earth-abundant compounds for practical applications. The strategies for the fabrication of defect-engineered TMDs summarized in this minireview and our rational understanding in this research field should provide inspirations for the design of the state-of-the-art catalysts for future developments in electrocatalytic HER. We hope that this minireview is helpful for the interested readers to have better understanding on the most recent advancements in the defect engineering of TMDs.

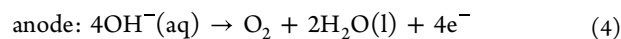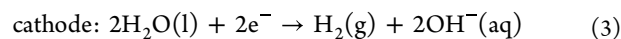## 2.0. ELECTROCATALYTIC WATER SPLITTING

### 2.1. Fundamentals of Electrocatalytic Water Splitting.
Water electrolysis is made up of two half-reactions, which are HER at the cathode and the oxygen evolution reaction (OER) at the anode.

Under acidic conditions, the following half-reactions occur:

$$\text{cathode: } 2H^+(aq) + 2e^- \rightarrow H_2(g) \tag{1}$$

$$\text{anode: } 2H_2O(l) \rightarrow O_2(g) + 4H^+(aq) + 4e^- \tag{2}$$
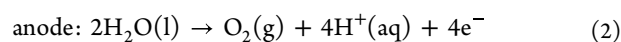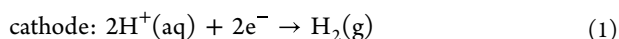
For neutral or alkaline conditions, the following half-reactions occur:

$$\text{cathode: } 2H_2O(l) + 2e^- \rightarrow H_2(g) + 2OH^-(aq) \tag{3}$$

$$\text{anode: } 4OH^-(aq) \rightarrow O_2 + 2H_2O(l) + 4e^- \tag{4}$$

The standard potentials of the half-reactions, measured relative to the standard hydrogen electrode (SHE), are presented in Table 1. By convention, half-reactions are written as reduction

**Table 1. Standard Redox Potentials of Half-Reactions in Water Electrolysis**

| half-cell reaction | $E^o$ |
| --- | --- |
| $2H^+ + 2e^- \rightarrow H_2$ | 0 V at pH 0 (by definition) |
| $O_2 + 4H^+ + 4e^- \rightarrow 2H_2O$ | +1.23 V at pH 0 |
| $2H_2O + 2e^- \rightarrow H_2 + 2OH^-$ | −0.83 V at pH 14 |
| $O_2 + 2H_2O + 4e^- \rightarrow 4OH^-$ | +0.40 V at pH 14 |

processes, even if the half-reaction occurs at the anode (i.e., oxidation), and the potentials are measured relative to the standard hydrogen electrode (SHE).

The overall cell potential, $E^o_{cell}$, is calculated by subtracting the $E^o$ of the oxidation half-reaction from the $E^o$ of the reduction half-reaction. The $E^o_{cell}$ of the water-splitting reaction is −1.23 V regardless of pH, as illustrated by eqs 5 and 6.

$$\text{for acidic condition: } E^o_{cell} = E^o_{cathode} - E^o_{anode} = 0 - 1.23$$
$$= -1.23 \text{ V} \tag{5}$$

$$\text{for alkaline condition: } E^o_{cell} = E^o_{cathode} - E^o_{anode}$$
$$= -0.83 - 0.4 = -1.23 \text{ V} \tag{6}$$

The negative $E^o_{cell}$ shows that the water-splitting reaction is overall nonspontaneous and thermodynamically unfavorable. A minimum voltage of 1.23 V needs to be applied to overcome the thermodynamic energy barrier for the reaction to occur.

Mechanistically, the HER is a multistep process as shown in Figure 1a. The HER begins with the Volmer step, where a proton binds to the catalyst and receives an electron to become an adsorbed H intermediate species. The proton source can be a hydronium cation (in acidic media) or a water molecule (in alkaline media). Subsequently, two coordinated H intermediates near each other can form a H−H bond and leave as a hydrogen ($H_2$) molecule, known as the Tafel step. Another possible desorption pathway is through the Heyrovsky step, where another proton binds to the H intermediate, receives an electron, and a $H_2$ molecule leaves.

According to the Sabatier principle, the rate of heterogeneous catalytic reactions depends on the binding strengths of the intermediates to the catalyst, and the optimal catalytic activity will be achieved with an intermediate binding strength that is not too strong and not too weak. The reactants and intermediates need to interact strongly enough with the catalyst to weaken the internal bonds and lower the activation energy of the reaction. However, if the intermediates bind too strongly, the active sites on the catalyst will be blocked because the products formed cannot desorb from the catalyst. For the HER, the binding strength of the hydrogen atom to the catalyst surface critically affects the catalytic performance. Hence, a volcano relationship (Figure 1b) exists between the free energy
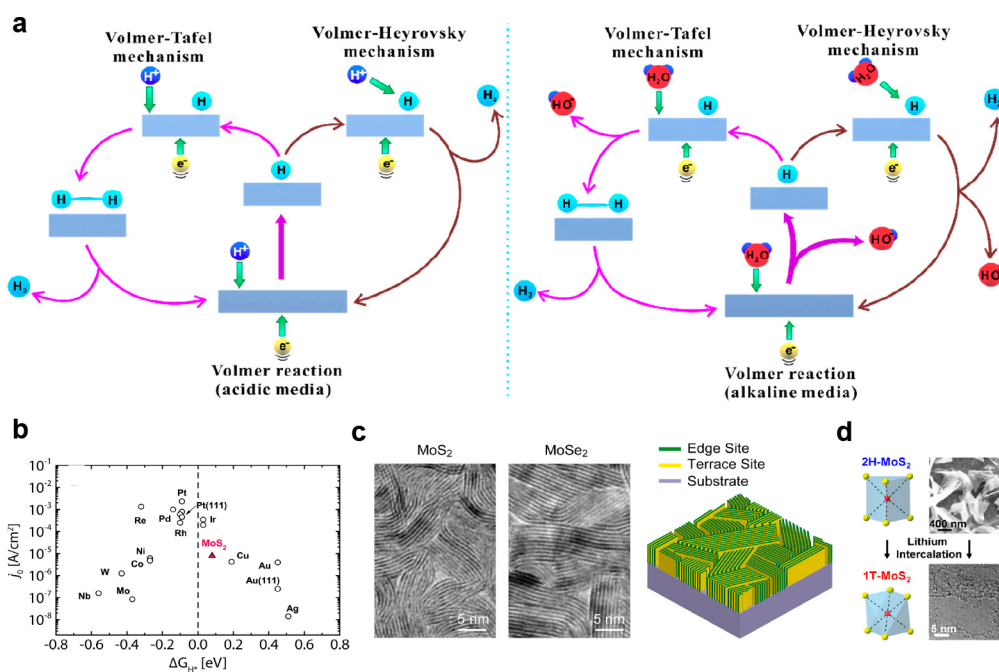
**Figure 1.** (a) Illustration of the HER mechanism in acidic (left) and alkaline conditions (right). Reprinted with permission from [5]. Copyright 2019 American Chemical Society. (b) Volcano plot showing the relationship between $\Delta G_{H*}$ and the HER activity (represented by $J_0$). Adapted with permission from [20]. Copyright 2014 American Chemical Society. (c) SEM images of vertically aligned $MoS_2$ (left) and $MoSe_2$ (middle) nanosheets, and an illustration of their orientation on the substrate (right). Reprinted with permission from [21]. Copyright 2013 American Chemical Society. (d) Illustration of the atomic rearrangement in the unit cell of $MoS_2$ and the change in morphology during the phase transformation from the 2H to the 1T phase by lithium intercalation. Reprinted with permission from [22]. Copyright 2013 American Chemical Society.

change of hydrogen adsorption ($\Delta G_{H*}$) and the exchange current density ($j_0$), which measures the binding strength and catalytic activity, respectively.[20] For an ideal electrocatalyst, its $\Delta G_{H*}$ should be zero along with the highest HER $j_0$.[23] Although noble metals such as Pt, Rh, Pd, and Ir display nearly neutral $\Delta G_{H*}$ accompanied by high $j_0$, their limited availabilities and high costs curtail their practical applications. In contrast, the earth-abundant and inexpensive $MoS_2$ exhibits nearly neutral $\Delta G_{H*}$ ($\Delta G_{H*} = 0.08$ eV with 50% coverage of H) and relatively high $j_0$ compared to a wide of range of metals,[17] making it a suitable candidate for the replacement of PGMs. Other than $MoS_2$, many TMDs are also reported as high-performance HER electrocatalysts, which will be discussed later.

## 2.2. Key Parameters for Evaluating the HER Catalysts.
In this section, the key parameters to evaluate electrocatalytic performances are briefly discussed to give the readers new to this area some foundational understanding. Interested readers are encouraged to refer to other comprehensive reviews for more thorough discussions on the experimental considerations in electrocatalyst benchmarking.[24,25]

The overpotential refers to the difference between the actual applied voltage to reach a particular benchmark current density (conventionally 10 mA/cm$^2$, $\eta_{10}$), and the thermodynamically required Nernstian potential, as shown in eq 7.

$$\eta = E_{app} - E_n \tag{7}$$

where $\eta$ is the overpotential, $E_{app}$ is the voltage applied, and $E_n$ is the Nernstian potential.

The excess voltage represents the additional energy input needed to overcome the activation energy barrier for the reaction to proceed at meaningful rates and to compensate for

energy losses due to the resistance of the various components in the electrochemical cell and the charge transfer resistance. A high-performing catalyst is characterized by having a low overpotential. In the case of a low-performing catalyst that has a higher overpotential, a larger voltage must be applied to sustain the same current density, thus consuming more electrical power (which is proportional to both voltage and current) to attain the same hydrogen production rate (proportional to current only), which leads to an overall less efficient conversion of electrical energy to chemical energy.

The Tafel slope is another pivotal parameter to evaluate the HER performance of a catalyst. The Tafel slope is the gradient of the linear part of the Tafel plot, which is obtained by plotting the overpotential versus the common logarithm of the current density. The Tafel equation (eq 8) is a limiting case of the Butler−Volmer equation, which describes the kinetics of electrochemical reactions, at large overpotentials where the reaction becomes irreversible.

$$\eta = b\log \frac{j}{j_0} \tag{8}$$

where $\eta$ is the overpotential, $j$ is the current density, $j_0$ is the exchange current density, and $b$ is the Tafel slope in the unit of mV/dec.

The Tafel equation is sometimes rearranged and conveniently expressed in the form of eq 9.[26]

$$\eta = a + b\log j \tag{9}$$

where $\eta$ is the overpotential, $a$ is a constant, $j$ is the current density, and $b$ is the Tafel slope in the unit of mV/dec.

The Tafel slope represents the increase in voltage needed for a 10-fold increase in the current density, and the value of the

Tafel slope can provide insights into the dominant HER mechanism and the rate-determining step for the electrocatalyst.[27] The exchange current density, $j_0$, can be determined from the Tafel plot by extrapolating the value of $\log j$ to the point when $\eta = 0$ mV. $J_0$ is a measure of the intrinsic activity of the catalyst under reversible conditions. A good electrocatalyst possesses a high exchange current density and a small Tafel slope, which means that there will be a large increase in current density following a small increase in the applied overpotential.

The charge-transfer resistance ($R_{ct}$) refers to the resistance of the interfacial charge transfer at the electrode surface. $R_{ct}$ is derived from the Nyquist plots obtained by electrochemical impedance spectroscopy (EIS). Typically, a low $R_{ct}$ is necessary for efficient catalysis.

The stability of the catalyst is also an important parameter to evaluate for the practical deployment of a HER electrocatalyst. Obviously, if the performance of the catalyst degrades within a short period of time and the catalysts need to be replaced or regenerated, it is not suitable for large-scale water electrolysis. Stability is typically determined by measuring the change in overpotential after multiple repetitive cyclic voltammetry scans (e.g., 10 000 CV scans) or prolonged (e.g., 24 h) constant-current electrolysis. A negligible increase in the overpotential required to maintain the same current density signifies that the catalyst is stable. Similarly, the decrease in current density attained should be negligible for a stable catalyst undergoing prolonged constant-potential electrolysis. Repetitive potential cycling scans simulate the startup and shutdown conditions in an electrolyzer, which serves as a harsher and faster way to determine the stability of the catalyst, whereas prolonged constant potential or constant current electrolysis are more representative for long-term operations.[16]

The turnover frequency (TOF) is an important parameter to evaluate the intrinsic catalytic activity of an electrocatalyst. TOF was first proposed by Michel Boudart back in year 1968, in which the TOF evaluates the number of molecules reacting per catalytic site in every second.[28] In modern electrochemistry, TOF was redefined as the total number of molecules that chemically converted into a desired product per active site per unit time.[29] The TOF can be expressed in the form of eq 10.[29]

$$TOF = \frac{jA}{4nF} \qquad (10)$$

where $j$ is the measured current density, $A$ is the geometric area of the working electrode, $n$ is the number of moles of active materials calculated using the electrochemically active surface area (ECSA) of the catalyst, and $F$ is the Faraday constant of 96 485.3 C mol$^{-1}$. Nevertheless, it is challenging to precisely quantify the TOF value for most solid-state electrocatalysts, especially those complex ones as some of the surface atoms in a catalyst are catalytically inactive or unequally accessible. Despite this, TOF is still a useful approach to compare the catalytic activities of numerous electrocatalysts, especially within a similar system.

## 3. DEFECT ENGINEERING OF TRANSITION METAL DICHALCOGENIDES (TMDS)

### 3.1. Introduction to Defect Engineering.
A crystalline defect refers to a lattice irregularity that has one or more of its dimensions on the order of an atomic diameter, in contrast to an idealized crystal lattice, which has infinitely many repeating unit cells with perfectly reproduced stoichiometry and lattice

parameters on the atomic scale.[30] Historically, the presence of crystalline defects in materials are often undesired. However, with the aid of more advanced characterization tools and fundamental theoretical calculations carried out in recent years, defect engineering has been discovered to be an effective approach to tune the chemical properties and catalytic activities for a myriad of nanomaterials. Generally, defects can be classified into four categories based on their dimensionality: 0D point defects, 1D linear defects, 2D interfacial defects, and 3D bulk defects. Point defects include atomic vacancies, where a normally occupied lattice site is missing an atom, or there may be substitutional foreign atoms, interstitial foreign atoms, and adatoms, which are atoms adsorbed on the surface but are not part of the lattice.[31] Linear defects include dislocations where some of the atoms are misaligned in the lattice. Interfacial defects include external surfaces, which have coordinatively unsaturated atoms that are not bonded to the maximum number of atoms, and grain and phase boundaries, which separate the individual crystallites in a polycrystalline material and different phases of materials, respectively. Bulk defects are defects larger than the atomic scale, such as pores and cracks.

Defect engineering, where a precise and controlled amount and type of a defect is deliberately introduced into materials, is beneficial for enhancing the desired properties of various nanomaterials. For example, defect engineering facilitates artificial tuning of the bandgap and extending the photoabsorption range of catalysts. These can in turn increase the electron mobility of defected semiconductors, and the surface defect sites normally serve as the active sites for heterogeneous catalysis to take place.[32−34]

Defect engineering presents an attractive alternative to surface structure and phase engineering to enhance the HER catalytic activity of TMDs. As introduced in section 1.0, in 2D TMDs such as MoS$_2$, the basal plane is inert and only the edge sites are catalytically active. The thermodynamically stable 2H phase of MoS$_2$, being a semiconductor, also has limited electron mobility which further handicaps the HER performance.[35] During the conventional synthesis of MoS$_2$, the basal plane would be preferentially exposed as the surface energy of the edge is much larger than the basal plane.[36] Surface structure engineering, such as growing vertically aligned TMD nanosheets (Figure 1c), can be effective in increasing the exposure of catalytically active edge sites.[21,37,38] Nonetheless, the intrinsic HER activity and electron mobility remains unchanged. 2H-MoS$_2$ can also be converted to the metallic 1T phase, as shown in Figure 1d, which has catalytically active basal planes and better charge transfer kinetics, resulting in improved HER performances.[22,39] However, 1T-MoS$_2$ is only metastable and will slowly convert back to the more stable 2H phase, and the synthesis usually involves harsh conditions, which restrict its suitability as a replacement for PGMs in large-scale water electrolysis.[40] In contrast, defect engineering can achieve the same benefits of both surface structure and phase engineering, including increasing the density of active sites available for catalysis, increasing electron mobility, and tuning of electronic structure to lower the $\Delta G_{H*}$, without limitations such as poor stability. For TMDs, the commonly encountered defects include chalcogen vacancies (i.e., sulfur/selenium vacancies), substitutional and interstitial foreign atoms, interfacial defects at the phase boundaries of heterostructures, and lattice distortions induced by vacancies and dopant atoms.
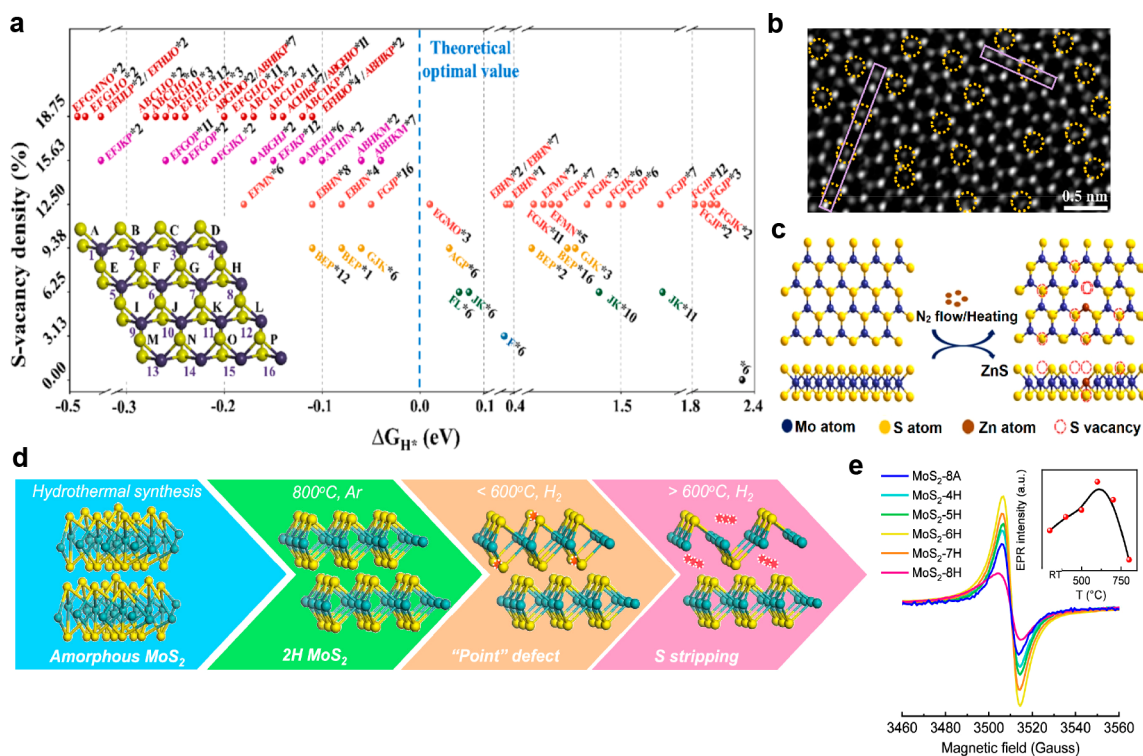
**Figure 2.** (a) The estimated $\Delta G_{H*}$ under various sulfur vacancy concentrations and the distribution in the lattice based on the DFT calculations. Reprinted with permission from [46]. Copyright 2020 American Chemical Society. (b) STEM image showing uniformly distributed single S-vacancies (yellow dotted circles) in a $MoS_2$ film after etching with $H_2O_2$. Reprinted with permission from [46]. Copyright 2020 American Chemical Society. (c) A scheme illustrating the reaction between $MoS_2$ and Zn to introduce S-vacancies. Reprinted with permission from [49]. Copyright 2019 John Wiley and Sons. (d) Illustration for the formation of S-vacancies in $MoS_2$ at a moderate annealing temperature in hydrogen, and stripping of S atoms to reveal large areas of undercoordinated Mo atoms at higher temperatures. Reprinted with permission from [50]. Copyright 2019 American Chemical Society. (e) EPR spectra of $MoS_2$ after annealing at various conditions. The inset shows the EPR intensity at different annealing temperatures. Reprinted with permission from [50]. Copyright 2019 American Chemical Society.

To support the existence of these defects in the TMDs, various advanced spectroscopy and microscopy techniques have been employed. Spectroscopy characterization such as X-ray photoelectron spectroscopy (XPS), X-ray absorption spectroscopy (XAS), electron spin resonance (ESR), and positron annihilation spectroscopy (PAS) are useful tools to disclose the chemical states, elemental compositions, atomic arrangements, and electronic structures of the nanomaterials. For 2H TMDs, XPS can be used to divulge the concentration and distribution of chalcogen vacancies. For example, when the S-vacancies in the 2H $MoS_2$ vary from point defects at lower concentration to higher concentration of aggregated states, a new doublet will emerge in the high-resolution Mo 3d spectrum, which manifests the presence of the under-coordinated Mo edges in the $MoS_2$ basal planes.[22] Recently, the use of synchrotron radiation XAS has explored to quantitatively study the oxidation states at the vacant sites, as well as the coordination numbers and configurations and bond lengths.[41] Other spectroscopy characterization techniques such as ESR and PAS are also useful to detect the changes in electronic structures induced by the defects. The S paramagnetic signal from ESR corresponds to the contribution of Mo−S dangling bonds, where a stronger signal implies a lower concentration of chalcogen atomic defects.[42] PAS can serve as subsidiary information for the existence of cation vacancies. From positron lifetime spectrum, the predominant shorter component corresponds to the lifetime of bulk component, whereas the defects in the materials contribute

to the longer life component.[43] Based on the relative intensity, the relative concentration of defects can be postulated. Other than the spectroscopy characterization, microscopy characterization based on transmission electron microscopy (TEM), scanning tunneling microscopy (STM), and atomic-resolution aberration-corrected high-angle annular dark-field scanning transmission electron microscopy (AC-HAADF-STEM) can also provide strong evidence for the presence of defects in TMDs. The high-resolution TEM (HRTEM) and STM can provide images for heterogeneous interface of TMDs at atomic-resolution.[44] In addition, the concentration and type of vacancies can be determined by AC-HAADF-STEM, in which the single Mo-vacancy, single S-vacancy, and double S-vacancy on $MoS_2$ are distinguishable.[45]

**3.2. Formation of Sulfur Vacancies in MoS₂.** For $MoS_2$, inducing sulfur vacancies (S-vacancies), which are highly beneficial to the HER catalytic activity, is a widely reported defect engineering approach. S-vacancies can be introduced by various methods including $H_2O_2$ etching,[46] reduction by $NaBH_4$,[47] addition of foreign elements, such as selenium[48] and zinc,[49] and annealing in a reducing[50] or inert atmosphere.[51] DFT calculations (Figure 2a) predicted that an optimized concentration of S-vacancies reduces the $\Delta G_{H*}$. Furthermore, an optimal S-vacancy concentration of 12.5% can lower the $\Delta G_{H*}$ to 0.02 eV, and single S-vacancies lead to smaller $\Delta G_{H*}$ than agglomerated S-vacancies at that concentration.[46] As explained in section 2.1, a small $\Delta G_{H*}$ is beneficial for HER activity. In addition, S-vacancies also serve as

catalytically active sites, and MoS$_2$ catalysts with S-vacancies exhibit higher measured electrochemically active surface area (ECSA) than their pristine counterparts.[46−50] Moreover, the $R_{ct}$ of MoS$_2$ can also be reduced by the formation of S-vacancies, leading to better HER performances.[46,48−50] More importantly, the presence of S-vacancies changes the rate-determining step from the adsorption step to the desorption step, which can be deduced from the stark decrease in the Tafel slope from ~120 mV/dec to ~50 mV/dec.[46−48]

Hydrogen peroxide (H$_2$O$_2$) chemical etching enables homogeneously distributed single atom S-vacancies to form on the surface of hydrothermal synthesized MoS$_2$ nanosheets, with excellent control of the S-vacancy concentration, as shown in Figure 2b. The best-performing catalyst with optimal S-vacancy concentration synthesized using this method required an overpotential of 131 mV to reach the benchmark 10 mA/cm$^2$ with a small Tafel slope of 48 mV/dec.[46] In comparison, the pristine MoS$_2$ without S-vacancies needed a larger overpotential of 220 mV to reach 10 mA/cm$^2$ along with a large Tafel slope of 121 mV/dec. This signifies the switch of the rate-limiting step from the Volmer discharge reaction to the Heyrovsky reaction. The trend of the experimentally measured HER performance of catalysts with various S-vacancy concentrations is in well agreement with the DFT simulation. MoS$_2$ with S-vacancies can also be synthesized by treatment with sodium borohydride (NaBH$_4$), a reducing agent. Although NaBH$_4$ treatment does not allow fine control of the distribution of the S-vacancies, the defects like lattice distortions and increased exposure of edge sites were present as well.[47] Solvothermally synthesized MoS$_2$ with a one-dimensional hierarchical architecture exhibited an excellent overpotential of 119 mV at 10 mA/cm$^2$ and a Tafel slope of 50.7 mV/dec after treatment with NaBH$_4$. More importantly, this S-deficient MoS$_2$ demonstrated long-term stability, where the current density remained stable after 24 h of reaction at an overpotential of 200 mV. In addition, the LSVs of the electrocatalyst deviated by only ~11 mV at the current density of 10 mA/cm$^2$ after 1000 repeated cycles.

Introduction of S-vacancies can be assisted by other elements such as selenium and zinc. Uniformly distributed, isolated S-vacancies can be formed on MoS$_2$ by annealing Se-doped MoS$_2$ to remove the Se atoms. The resulting MoS$_2$ with uniformly distributed and isolated S-vacancies that were hydrothermally synthesized by deselenization of Se-doped MoS$_2$ (MoS$_{1.76}$Se$_{0.24}$) needed an overpotential of only 100 mV to attain a current density of 10 mA/cm$^2$ with a Tafel slope of 49 mV/dec.[48] Compared to the MoS$_2$ with single-atom S-vacancies formed by H$_2$O$_2$ etching, the deselenized MoS$_2$ has a smaller overpotential. Bulk MoS$_2$ can also be reduced by Zn powder to form Zn-doped MoS$_2$ with sulfur vacancies, as shown in in Figure 2c.[49] ZnS and elemental Mo are formed as byproducts, and the MoS$_2$ nanosheets were observed to decrease in lateral size, likely due to the lateral cracking of the MoS$_2$ nanosheets during the exothermic reaction with Zn. DFT calculations simulated that by substituting the Mo atoms with Zn atoms, the formation energy of the S-vacancies near the Zn atom was reduced from ~2.2 eV to ~0.64 eV, enabling S-vacancies to form more easily. In addition, the S-vacancy sites adjacent to Zn atoms have smaller $\Delta G_{H*}$. The Zn dopants and metallic Mo present also contribute to the overall reduction of $R_{ct}$. In comparison with pristine MoS$_2$, Zn-doped MoS$_2$ with an optimal S-vacancy concentration has a 28-fold increase in ECSA, a 63% smaller Tafel slope (73 mV/

dec vs. 199 mV/dec), and a 64% smaller overpotential required to reach 10 mA/cm$^2$ (194 mV vs. 540 mV).

DFT calculations predict that the $\Delta G_{H*}$ increases at higher concentrations of S-vacancies, which supposedly results in poorer HER performance. However, when solvothermal grown MoS$_2$ nanosheets were annealed in a reducing atmosphere (5% hydrogen) at different temperatures between 400 and 800 °C, the HER performances continued to improve as the S:Mo ratio decreased, as reflected by the decreasing overpotentials and increasing turnover frequencies (TOFs). The undercoordinated Mo regions instead of the S-vacancies were proposed to be responsible for the improved HER performances at lower S:Mo ratios, thus explaining this observed trend. Below 600 °C, the S vacancies (point defects) formed were primarily responsible for the improvement in HER activity, whereas at higher temperatures, large areas of S atoms were stripped and undercoordinated Mo regions were exposed, as shown in Figure 2d. Sulfur vacancies can be detected by electron paramagnetic resonance (EPR) since the Mo−S dangling bonds contain unpaired electrons. As the H$_2$ annealing temperature increased from 400 to 600 °C, the intensity of the EPR signal induced by the S-vacancy increased, providing evidence for the increase in S-vacancy concentrations. The EPR signal intensity peaked at 600 °C and decreased as the annealing temperature increased, as shown in the Figure 2e inset, indicating that at the higher temperatures, the defects were no longer point defects with Mo−S dangling bonds but were instead larger areas of undercoordinated Mo atoms. The presence of undercoordinated Mo atoms was further supported by XPS data. A similar work that involved annealing CVD-grown MoS$_2$ nanoplatelets in 20% H$_2$ between 600 and 800 °C also discovered the formation of bulk defects observable by SEM, such as roughened and serrated nanoplatelet edges, whereas nanopores and nanoribbons were formed at higher temperatures.[52]

Frenkel defects are formed when an atom leaves its original position in the lattice and gets lodged in an interstitial position, resulting in a vacancy and an interstitial defect at the same time. Frenkel-defected monolayer MoS$_2$ could be formed by annealing CVD-grown monolayer MoS$_2$ in an inert atmosphere (argon gas) at 400 °C.[51] The presence of the Frenkel defects were confirmed by atomic-resolution HAADF-STEM, and DFT calculations revealed that the preferred H adsorption site is between the interstitial Mo atom and the nearby Mo atom, with a $\Delta G_{H*}$ of 0.36 eV compared with 2.03 eV of pristine monolayer MoS$_2$. The electrocatalytic activity of Frenkel-defected MoS$_2$, measured in a microelectrochemical cell, was considerably superior to that of pristine monolayer MoS$_2$ and even Pt-doped MoS$_2$. The optimized Frenkel-defected MoS$_2$ required an overpotential of 164 mV to reach 10 mA/cm$^2$ with a remarkably small Tafel slope of 36 mV/dec; in comparison, the Pt-doped MoS$_2$ needed a larger over-potential of 211 mV and exhibited a steeper Tafel slope of 105 mV/dec.

### 3.3. Formation of Selenium Vacancies in MoSe$_2$.

Selenium vacancies (Se-vacancies) are highly beneficial to the HER performance of MoSe$_2$, analogous to S-vacancies for MoS$_2$ explained in the preceding section. Se-vacancies in MoSe$_2$ are typically induced by substitution of Mo atoms by metal dopant atoms such as manganese (Mn),[53] niobium (Nb),[54] and vanadium(V),[55] which reduce the formation energy of the Se-vacancies.
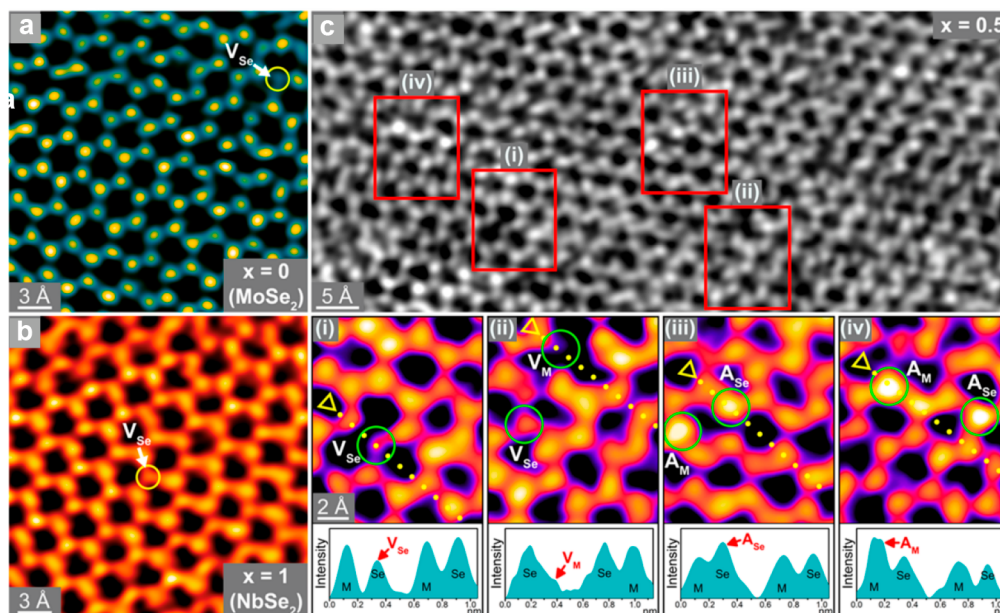
**Figure 3.** Atomically resolved HAADF-STEM images of (a) MoSe$_2$, (b) NbSe$_2$, and (c) Mo$_{0.5}$Nb$_{0.5}$Se$_2$. The insets of (c) show the intensity profiles across the yellow dotted lines. V$_{Se}$, V$_M$, A$_{Se}$, and A$_M$ represent the Se-vacancy, the metal-vacancy, the adatom at the Se site, and the adatom at the metal site, respectively. Reprinted with permission from [54]. Copyright 2021 American Chemical Society.

Depending on the location of the Se-vacancy, DFT calculations showed that the formation energy of Se-vacancies is reduced by a range of 0.12−0.80 eV after Mn substitutional doping.[53] With the optimized Mn loading of 2.4%, the $R_{ct}$ was reduced by 75% and the ECSA was tripled compared to pristine MoSe$_2$. Thus, the resulting overpotential needed to reach 10 mA/cm$^2$ in acidic solutions was reduced to 167 mV with a Tafel slope of 60 mV/dec, along with excellent stability where no significant changes to the catalytic current density was observed in the polarization curves after 2000 CV cycles in 0.5 M H$_2$SO$_4$. This remarkable HER activity for the Mn-doped MoSe$_2$ was largely attributed to the promotion of Se-vacancy formation, instead of electron donation by the $n$-type dopant Mn. DFT calculations found that despite the reduction in $\Delta G_{H*}$ by the effects of doping, the $\Delta G_{H*}$ on the MoSe$_2$ basal plane was still too large for efficient catalysis ($\Delta G_{H*}$ = +1.06 eV), whereas the $\Delta G_{H*}$ on the Se-vacancy sites were much closer to the ideal value of 0 ($\Delta G_{H*}$ = −0.12 eV to −0.06 eV).

MoSe$_2$ benefits from substitutional doping by $p$-type dopants like Nb and V (both group 5 elements) as well, since the main effect of the metal dopant is to promote the formation of Se-vacancy sites. In V-doped MoSe$_2$, the composition Mo$_{0.7}$V$_{0.3}$Se$_2$ exhibited the highest HER catalytic activity in acidic solutions, requiring an overpotential of only 114 mV to reach 10 mA/cm$^2$ with a Tafel slope of 43 mV/dec On the other hand, in alkaline solutions, Mo$_{0.6}$V$_{0.4}$Se$_2$ had the best HER performance, requiring an overpotential of 157 mV to reach 10 mA/cm$^2$ with a Tafel slope of 76 mV/dec.[55] Theoretically, the formation energies for Se- and V-vacancies reached a minimum of 1.30 eV for Se-vacancies (cf. 2.35 eV in pristine MoSe$_2$) and 3.90 eV for V-vacancies in Mo$_{0.5}$V$_{0.5}$Se$_2$. Various characterization techniques including atomically resolved HAADF-STEM, EDX, XPS, and ICP-AES revealed that the abundance of V- and Se-vacancies were the highest when $x$ = 0.3−0.5 (Mo$_{1-x}$V$_x$Se$_2$), coinciding to the compositions with the highest HER performance. The DFT calculations suggested that in the presence of V-vacancies, the

$\Delta G_{H*}$ of a H atom bonded to a neighboring Se atom is only −0.05 eV. Similarly, the $\Delta G_{H*}$ of a H atom occupying a Se-vacancy adjacent to a V-vacancy site and bonded with three adjacent V atoms is 0.15 eV, accounting for the superior HER performance. For Nb-doped MoSe$_2$, the composition Mo$_{0.5}$Nb$_{0.5}$Se$_2$ required the lowest overpotential of 140 mV to reach 10 mA/cm$^2$ with a Tafel slope of 46 mV/dec in acidic solutions.[54] The HAADF-STEM images of MoSe$_2$ (Figure 3a) and NbSe$_2$ (Figure 3b) disclosed the well-defined hexagonal atomic arrangements of Mo (or Nb) and Se atoms. Meanwhile, the HAADF-STEM (Figure 3c) and EPR revealed that the composition Mo$_{0.5}$Nb$_{0.5}$Se$_2$ correspondingly had the highest concentrations of Nb- and Se-vacancies at 4.7% and 7%, respectively. Adatoms were also found on both the metal and Se sites with a concentration of 5%. DFT calculations suggested that the most favorable catalytic sites were the Se-vacancy sites, where the H atom forms Mo−H and Nb−H bonds ($\Delta G_{H*}$ = −0.01 eV), simultaneous Nb/Se-vacancy sites where the H atom bonds with two Nb and one Mo atom in the NbSe$_2$−MoSe$_2$ domain boundary ($\Delta G_{H*}$ = −0.03 eV), and the Nb adatoms ($\Delta G_{H*}$ = −0.03 eV) where the H atom forms a Nb−H−Nb bridge bond.

## 3.4. Defects from Foreign Atoms Doping and the Heterostructures.

In addition to artificially induced vacancies, doping of foreign atoms can also induce point defects. Other than modulating the electronic structures of MoS$_2$, the dopant atoms will promote the intrinsic HER activity by bringing the $\Delta G_{H*}$ closer to zero and increasing the electron density and electron mobility. Owing to the differences in the atomic radii of the dopant atoms and the original atoms in the lattice, the defects such as atomic vacancies and lattice distortions are commonly found in doped MoS$_2$. MoS$_2$ is typically $n$-type doped with elements having more valence electrons than Mo, such as iron (Fe, Group 8),[56] cobalt (Co, Group 9),[57] and phosphorus (P, Group 15),[58] to enhance its HER performance, whereas $p$-type doping is likely to negatively affect the HER performance instead.[59] After the

creation of defect sites through foreign atoms doping, the doped $MoS_2$ can also be incorporated with other materials such as nitrogen-doped carbon, nickel hydroxide, or cobalt sulfide to form heterostructures with versatile catalytic properties, in which the phase boundary is also a type of interfacial (2D) defect with abundant potential catalytically active sites.

Recently, Co-doped $MoS_2$ were reported to grow on highly conductive Ketjen black nanoparticles by a solvothermal reaction using a polyoxomolybdate ($(NH_4)_3PMo_{12}O_{40}$) as the Mo source, $Co(NO_3)_2 \cdot 6H_2O$ as the Co source, and thioacetamide ($C_2H_5NS$) as the S source.[57] A decrease in the Mo 3d binding energy was observed in the XPS, indicating that the $n$-type Co dopants increased the electron density on the Mo atoms, hence increasing the rate of the Volmer step. The Co dopants also reduced the crystallinity of the $MoS_2$ and enhanced the exposure of catalytically active groups. The Co-doped catalyst needed an overpotential of 81 mV to reach 10 mA/cm$^2$ under alkaline conditions and exhibited a Tafel slope of 64 mV/dec, demonstrating a significant improvement over pristine $MoS_2$. This result is fascinating as the $MoS_2$-based electrocatalysts generally suffer from poor performances in high pH, but Co-doping enables $MoS_2$ to be an efficient HER catalyst in both neutral and alkaline conditions.[60] Besides, sulfurization of $CoMoO_4$ forms porous $CoS_{1.097}/MoS_2$ hybrid microspheres, which exhibit a lower overpotential, Tafel slope, and $R_{ct}$ than undoped $MoS_2$ and $CoS_{1.097}$ in both pH 7 (neutral) and 14 (alkaline) solutions.[60] HRTEM revealed the presence of crystalline defects at the heterogeneous interface of $CoS_{1.097}$ and $MoS_2$, and the ECSA of $CoS_{1.097}/MoS_2$ was higher than that of pristine $MoS_2$ by a factor of 29.

The formation of heterostructures by growing $MoS_2$ on nitrogen-doped carbon substrates leads to the formation of Mo−N bonds that enhance the intrinsic HER activity of $MoS_2$. In addition, the high electrical conductivity and large surface area of nitrogen-doped carbon substrates facilitate charge and mass transfer, respectively, further improving the overall HER performances. Xia et al. found that iron-doping of $MoS_2$ encapsulated by nitrogen-doped carbon further decreased its Tafel slope to 67 mV/dec, increased its ECSA by 112%, and decreased the $R_{ct}$ by 69% from 29 Ω to 9 Ω.[56] The presence of the Fe atoms led to larger interlayer spacing and fewer layers in the nanosheet, and also embedded to the basal plane of $MoS_2$ for the formation of high density doping and vacancy defects. This regional active site regulation renders more active sites for HER and enhanced the intrinsic electrocatalytic activity of the catalyst. Furthermore, the strategic coupling of iron-doped $MoS_2$ with nitrogen-doped carbon layer allows the highly active iron-doped $MoS_2$ to be protected by the nitrogen-doped carbon layer, leading to excellent stability for HER, as evidenced by its long-term stability of 12 h for HER. Other types of defects, such as Mo- and S-vacancies, and lattice distortions were present as well. DFT calculations revealed that the formation of Mo−N bonds with the nitrogen-doped carbon nanosheets can redistribute the charge between the N and Mo atoms and reduce the $\Delta G_{H*}$, which is further optimized by Fe-doping. Zhao et al. synthesized phosphorus-doped $MoSe_xS_{2−x}$ on nitrogen-doped carbon nanotubes grown on carbon cloth, resulting in an optimized catalyst with the composition P-doped $MoSe_{0.5}S_{1.5}$.[58] XPS data suggested the presence of N−Mo bonds, which enhance the intrinsic HER activity as the lone-pair electrons on the pyridinic N atoms are favorable for proton adsorption, and the strong catalyst-

substrate interactions improve the morphology of the active catalyst and prevent aggregation of the nanosheets. In the composition with the optimized Se:S ratio, $MoSe_2/MoS_2$ heterojunctions are beneficial to the HER performance. After P-doping, the HER activity is further enhanced as the excess valence electrons in P can form strong covalent bonds with the surrounding valence electrons, while the intrinsic electrical conductivity of the catalyst is enhanced owing to the free electrons formed from the excess valence electrons. In addition, the mismatch between the size of P and S atoms induces the formation of defects such as lattice distortions in the crystal structure, which increase the number of catalytically active sites. The various factors such as electronic structure modulation, defect formation, large catalytically active surface area, and high electrical conductivity work synergistically to enable the optimized catalyst to reach 10 mA/cm$^2$ with an overpotential of 108.3 mV and a Tafel slope of 58.6 mV/dec.

In addition to increasing HER activity, heterostructures can confer bifunctionality to $MoS_2$, allowing it to catalyze both the HER and the OER. The bifunctional $Ni(OH)_2/MoS_2$ heterostructure catalyst can be synthesized by irradiating the $MoS_2$ nanosheets with $Ar^+$ ions to create S-vacancies on the nanosheets, followed by immersion of the defect-containing nanosheets in nickel acetate solution to deposit $Ni(OH)_2$, where the S-vacancies promote $Ni^{2+}$ ion adsorption on the $MoS_2$.[61] The heterostructured catalyst with irradiated $MoS_2/Ni(OH)_2$ containing the S-vacancies has the smallest $R_{ct}$ requiring an overpotential of 139 mV to reach 10 mA/cm$^2$ for HER in alkaline solutions with a Tafel slope of only 45 mV/dec, lower than that of the $MoS_2$ sample with S-vacancies but without $Ni(OH)_2$, which needed an overpotential of 181 mV to reach 10 mA/cm$^2$. Meanwhile, the heterostructured sample with $Ni(OH)_2$ but without S-vacancies required an overpotential of 156 mV to reach 10 mA/cm$^2$. The improvement in HER performance was attributed to the effective transfer of electron density from $Ni(OH)_2$ to $MoS_2$. Concurrently, the $Ni(OH)_2$ also played a crucial role in efficiently catalyzing the dissociation of $H_2O$. The irradiated $MoS_2/Ni(OH)_2$ also exhibited good OER performance with a current density of 40.4 mA/cm$^2$ at 1.65 V vs. RHE, whereas the $MoS_2$ samples without $Ni(OH)_2$ had negligible OER activity, regardless of whether S vacancies were present. Similarly, the presence of S-vacancy rich $MoS_2$ improves the OER activity of $Ni(OH)_2$ by lowering the electron density on $Ni(OH)_2$ to facilitate the adsorption and oxidation of $OH^-$, and by promoting the deprotonation steps in the OER.

## 3.5. Synergistic Phase and Defect Engineering.
Phase engineering is a complementary strategy to defect engineering for improving the HER catalytic activity. This is because the metastable phases of 2D TMDs, such as the metallic 1T phase, typically have higher intrinsic catalytic activity, greater density of catalytically active sites, and better electrical conductivity compared to the thermodynamically favored 2H phase. The phase boundaries at the interface between the different phases are 2D defects as mentioned in section 3.1 and contain coordinatively unsaturated atoms, which serve as the active sites for the HER.

$MoS_2$ with coexisting 1T and 2H phases can be synthesized from orthorhombic $\alpha$-$MoO_3$ by hydrothermal sulfurization of $\alpha$-$MoO_3$ using thiourea.[62] In the optimized sample with ∼47% metallic 1T-$MoS_2$, 18% 2H-$MoS_2$, and 35% $\alpha$-$MoO_3$, the benchmark current density of 10 mA/cm$^2$ was achieved with an overpotential of 210 mV and a Tafel slope of 50 mV/dec
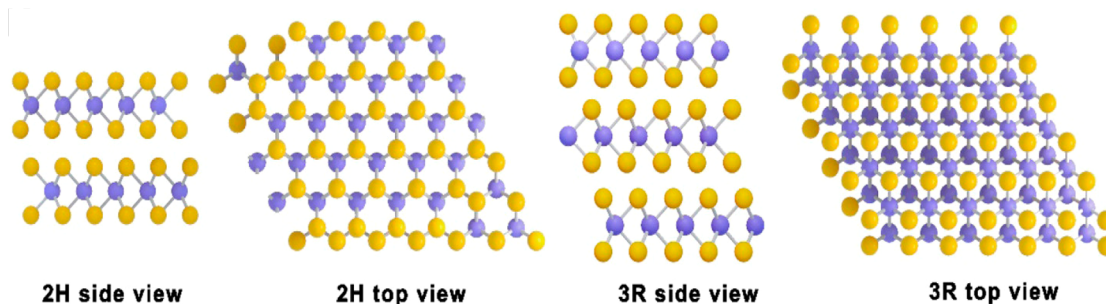
**Figure 4.** Illustration of the atomic arrangement in 2H- and 3R-MoS$_2$. Reprinted with permission from [64]. Copyright 2020 American Chemical Society.
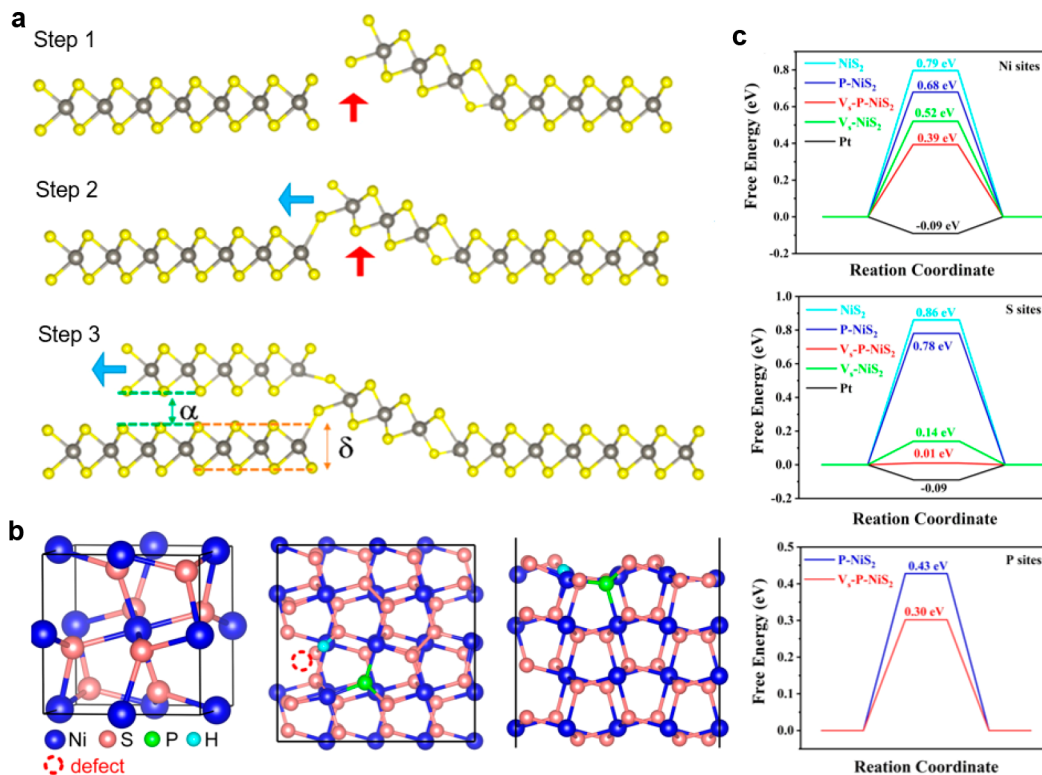


**Figure 5.** (a) Illustration for the growth mechanism of spiral WS$_2$. The single-layer thickness of WS$_2$ nanosheet and interlayer spacing of WS$_2$ layers are represented by $\delta$ and $\alpha$, respectively. Reprinted with permission from [66]. Copyright 2019 American Chemical Society. (b) The crystal structure (left) of pristine NiS$_2$, top view (middle) and side view (right) of the optimal binding site for H in P-doped NiS$_2$ with S-vacancies. (c) DFT calculations for the $\Delta G_{H*}$ of various possible binding sites of P-doped NiS$_2$ with S-vacancies. Reproduced with permission from [68]. Copyright 2021 Elsevier.

HRTEM analysis disclosed crystalline defects at the 1T/2H phase boundary and vacancy sites on the basal plane, while the measured ECSA of the optimized sample was nearly four times that of the 2H-MoS$_2$ sample since the defect sites are catalytically active. The selenium analogue, 1T/2H-MoSe$_2$ nanosheets, can similarly be synthesized by selenization of Anderson-type polyoxometalates.[63] HRTEM revealed that selenization of the polyoxomolybdate without other metal heteroatoms forms 2H-MoSe$_2$, whereas selenization of cobalt, iron, or nickel-containing polyoxomolybdate results in a mix of doped 1T and 2H-MoSe$_2$ with lattice disorder at the phase boundary. The synthesized Co-doped 1T/2H-MoSe$_2$ nanosheets required a low overpotential of 116 mV to reach 10 mA/cm$^2$ with a Tafel slope of 47 mV/dec in acidic solutions, and an overpotential of 274 mV to reach 10 mA/cm$^2$ with a Tafel slope of 142 mV/dec in simulated seawater. The HER

performance of the Co-doped 1T/2H-MoSe$_2$ in seawater even exceeded that of the model HER catalyst Pt/C at high overpotentials, suggesting that the Co-doped 1T/2H-MoSe$_2$ has potential applications in large-scale industrial water electrolysis. It is worth noting that the Co-doped 1T/2H-MoSe$_2$ cathode can also be combined with a magnesium anode to make a Mg/seawater battery that produces an electric current and H$_2$ concurrently.

Other than the 1T phase, the formation of the rhombohedral 3R phase in MoSe$_2$ is beneficial to its HER activity. In the 3R phase, the MoSe$_6$ prismatic polyhedrals in each layer are oriented parallel to one another, in contrast with the antiparallel orientation of the 2H phase, as illustrated in Figure 4. The 2H/3R-MoSe$_2$ can be grown on P-doped carbon prepared by a solvothermal reaction in *N,N*-dimethylformamide and hydrazine hydrate using the phosphorus-containing

phytic acid as the precursor for the P-doped carbon, and molybdenyl acetylacetonate and Se powder as the Mo and Se sources, respectively.[64] The phase transition from 2H to 3R is hypothesized to be due to the transfer of electron density from $MoSe_2$ to the P-doped carbon, which stabilizes the 3R phase. The 2H/3R-$MoSe_2$ exhibited an overpotential of 164 mV to reach 10 mA/cm$^2$ with a Tafel slope of 44 mV/dec Control experiments where the 3R phase is transformed back to the 2H phase by high-temperature annealing significantly deteriorated the HER performance, confirming the beneficial effect of the 3R phase. Due to the differences in the atomic arrangement between the 2H and the 3R phases, defect sites such as lattice distortion and expanded interlayer spacing were formed at the phase boundary, as observed by HRTEM.

### 3.6. Defect Engineering in Other Metal Dichalcogenides.

Defect engineering is a versatile strategy that can improve the electrocatalytic HER activities of a myriad of TMDs in addition to the more commonly reported molybdenum chalcogenides, including 2D layered TMDs like $WS_2$ and 3D TMDs like $NiS_2$.

Single atom S-vacancies can also be induced in hydrothermally synthesized $WS_2$ nanosheets by $H_2O_2$ etching,[65] similar to the case of $MoS_2$ discussed in section 3.2. Furthermore, the $WS_2$ nanosheets with S-vacancies were anchored to the surface of defective graphene to further enhance its HER activity, where the heterostructured catalyst needed a small overpotential of 108 mV to reach 10 mA/cm$^2$ with a Tafel slope of 48 mV/dec The ECSA of the heterostructure was almost three times than that of pristine $WS_2$ and the $R_{ct}$ was 61% lower. The successful formation of uniformly distributed single S-vacancies was confirmed by scanning tunneling electron microscopy and EPR spectroscopy. The formation of the heterojunction with defective graphene was hypothesized to enhance the HER activity by facilitating charge migration and accelerating the electron transfer. DFT calculations estimated that the $\Delta G_{H*}$ was reduced by a factor of almost four, from −1.62 eV in pristine $WS_2$ to −0.41 eV in S-deficient $WS_2$ coupled with defective graphene. Other than the point defects, linear defect formation is another effective approach to enhance the HER performance of $WS_2$. Spiral $WS_2$ domains can be formed by axial screw dislocation in the basal plane, which is a type of linear defect. Sarma et al. reported a controlled CVD technique for growing spiral $WS_2$, after which they found that the spiral $WS_2$ demonstrated better HER performance with a 33% lower Tafel slope and a lower onset potential in comparison to the CVD-grown monolayer $WS_2$.[66] As illustrated in Figure 5a, the growth mechanism of spiral $WS_2$ is initiated by an uplifting of a grain boundary due to the differential growth rates of various edge terminations of $WS_2$ in the CVD environment where there is a high concentration of precursors. The unsaturated sulfur atoms in the uplifted plane becomes the nucleation site where additional precursor atoms continue to bond, resulting in another layer of $WS_2$ growing above the bottom layer. Conductive-AFM measurements revealed that the spiral $WS_2$ has better electrical conductivity vertically, in the direction perpendicular to the basal plane. The enhanced HER performance of spiral $WS_2$ is attributed to a higher amount of catalytically active edge sites that facilitated vertical electron transportation.

In addition to the layered TMDs like $MoS_2$ and $WS_2$, nickel chalcogenides, which do not adopt a layered-structure, can also benefit from the defect engineering. The atomically thin nanosheets of $NiSe_{1.2}S_{0.8}$ showed better catalytic activity than solitary $NiS_2$ or $NiSe_2$, requiring an overpotential of 144 mV to reach 10 mA/cm$^2$ with a Tafel slope of 59 mV/dec in acidic condition.[67] The HRTEM image confirmed the presence of defects in the lattice due to the mismatch in the atomic radii of S and Se, accompanied by a reduction in the lattice spacing of the {210} facet of $NiSe_2$. The measured ECSA of $NiSe_{1.2}S_{0.8}$ was more than twice that of $NiSe_2$ and thrice that of $NiS_2$, implying that the defect sites were catalytically active. XPS analysis showed that the binding energies of the Ni 2p peaks of the $NiSe_{1.2}S_{0.8}$ are smaller than those of both $NiS_2$ and $NiSe_2$, indicating that the incorporation of both S and Se tunes the electronic structure of the material and increases the electron density on Ni. DFT calculations also predicted that the $\Delta G_{H*}$ of $NiSe_{1.2}S_{0.8}$ is −0.30 eV, much smaller than that of pristine $NiSe_2$ (0.565 eV), which leads to a higher intrinsic HER activity.

Furthermore, the HER activity of $NiS_2$ can also be boosted by phosphorus-doping. Phosphorus-doped $NiS_2$ can be synthesized by phosphidation of a $NiOOH/NiS_x$ precursor.[68] The optimized P-doped $NiS_2$ is a bifunctional electrocatalyst which catalyzes both the HER and OER, requiring a remarkably small overpotential of 73 mV to reach 10 mA/cm$^2$ in alkaline solutions with a Tafel slope of 87 mV/dec Furthermore, the optimized P-doped $NiS_2$ electrocatalyst demonstrated good long-term stability, in which the current density was maintained at 10 mA/cm$^2$ over a period of 12 h. This indicates that the P-doped $NiS_2$ catalyst possesses stable HER activity for 12 h, which is comparable to the commercial Pt/C electrocatalyst. This was attributed to the tuning of electronic structure of $NiS_2$ by the phosphorus dopants, where the electron density at the Ni cations decreasing while electron density at the S sites increasing. The phosphorus dopants also induced the formation of a variety of defects, such as S-vacancies, dislocations, lattice distortions, and nanoholes visible by TEM on the $NiS_2$ nanoplates. The abundant defects are beneficial to the HER activity as the defect sites are catalytically active, and the ECSA of the optimized P-doped $NiS_2$ was almost six times that of pristine $NiS_2$. The optimal binding sites for the H atom in the P-doped $NiS_2$ with S-vacancy were also simulated for comparison with the pristine $NiS_2$ (Figure 5b). From the DFT calculations in Figure 5c, the concurrent presence of P dopants and S-vacancies lower the $\Delta G_{H*}$ at the various possible binding sites for the H atom, with the smallest $\Delta G_{H*}$ = 0.01 eV at the S atom near the S-vacancy of P-doped $NiS_2$, even smaller than that of Pt. This implies that the P-doped $NiS_2$ with S vacancies should be highly active for HER.

## 4.0. SUMMARY AND OUTLOOK

This minireview summarizes the recent advancements of defect engineering for enhancing the electrocatalytic HER performance of TMDs, with some of the catalysts nearing or even exceeding the activity of the benchmark HER catalyst, Pt/C under research laboratory test conditions, bringing hope for low-cost and economically viable green $H_2$ production by water electrolysis. Defect engineering of TMDs can also be extended to other value-added cathodic reactions such as electrochemical $CO_2$ reduction into carbon-neutral fuels and nitrogen fixation into ammonia. However, for defect-engineered TMDs to be a viable replacement for Pt in industrial-scale water electrolysis, their catalytic activities need to be evaluated at industrially relevant overpotentials and

current densities that are required for commercially viable $H_2$ production rates. These current densities are usually much higher than the laboratory conditions, on the order of $A/cm^2$, compared with the usual benchmark current density of 10 mA/$cm^2$. Factors in addition to the cost and activity of the HER catalyst, such as the availability of water for electrolysis, the cost and accessibility of renewable generated electricity, the reactor design and catalyst substrate for efficient mass and charge transfer, and the cost and activity of the OER catalyst, need to be considered holistically as well. Nevertheless, the significant progress made recently on the development of defect-engineered TMDs for electrocatalytic HER demonstrates the potential of this class of material as a replacement for the expensive and rare noble metal catalysts. To bring the TMD-based electrocatalysts a big step toward the industrial applications, more intensive, in-depth, and systematical mechanistic investigations based on DFT calculations should be performed in order to provide more detailed and fundamental theoretical insights into the reaction mechanisms of HER over these defects and vacancies to offer rational guidance for designing next generation electrocatalysts. Since most of the conventional characterization approaches for HER electrocatalysts are *ex situ* techniques which do not provide information about the reaction intermediates adsorbed on the electrocatalysts surface during the reaction, more *in situ* and *operando* techniques should be developed to disclose more information about the active sites and surface layers of the electrocatalysts during HER to divulge the catalytic mechanisms. Till date, only a few members of TMD family (e.g., $MoS_2$, $MoSe_2$, $WS_2$, $WSe_2$, $NiS_2$, and $NiSe_2$) have been studied for electrocatalytic applications. Many of the TMD family members, especially those *d*-electron-rich noble-TMDs (e.g., $PtS_2$, $PtSe_2$, $PtTe_2$, $PdS_2$, $PdSe_2$, $PdTe_2$) were less developed and studied. To enrich the designability of TMDs for electrocatalytic $H_2$ evolution, new family members with unexplored crystal phases should be experimentally investigated to expand the TMD family. Other than the cost for electrocatalysts fabrication, the energy consumption for electrocatalytic $H_2$ production is another issue to be considered before the commercialization of water electrolysis. The configurations of water electrolyzers should be carefully designed, and ideally, they should be integrated with other devices such as photovoltaic cell to harness solar energy, or other power systems such as wind and tidal generator, to realize the industrial application of HER.

## AUTHOR INFORMATION

### Corresponding Authors
**Xin Ying Kong** − *School of Chemistry, Chemical Engineering and Biotechnology, Nanyang Technological University, Singapore 637371, Singapore*; Email: xinying.kong@ntu.edu.sg
**Siang-Piao Chai** − *Multidisciplinary Platform of Advanced Engineering, Chemical Engineering Discipline, School of Engineering, Monash University, 47500 Selangor, Malaysia*; orcid.org/0000-0002-8635-1762; Email: chai.siang.piao@monash.edu

### Authors
**Zheng Hao Tan** − *School of Chemistry, Chemical Engineering and Biotechnology, Nanyang Technological University, Singapore 637371, Singapore*

**Boon-Junn Ng** − *Multidisciplinary Platform of Advanced Engineering, Chemical Engineering Discipline, School of Engineering, Monash University, 47500 Selangor, Malaysia*
**Han Sen Soo** − *School of Chemistry, Chemical Engineering and Biotechnology, Nanyang Technological University, Singapore 637371, Singapore*; orcid.org/0000-0001-6502-2313
**Abdul Rahman Mohamed** − *Low Carbon Economy (LCE) Group, School of Chemical Engineering, Universiti Sains Malaysia, 14300 Nibong Tebal, Pulau Pinang, Malaysia*

Complete contact information is available at:
https://pubs.acs.org/10.1021/acsomega.2c06524

### Notes
The authors declare no competing financial interest.

## REFERENCES
(1) Kong, X. Y.; Lee, W. Q.; Mohamed, A. R.; Chai, S.-P. Effective Steering of Charge Flow through Synergistic Inducing Oxygen Vacancy Cascade : Towards Superior Photocatalytic $CO_2$ Reduction Activity. *Chem. Eng. J.* **2019**, *372*, 1183−1193.
(2) Welsby, D.; Price, J.; Pye, S.; Ekins, P. Unextractable Fossil Fuels in a 1.5 °C World. *Nature* **2021**, *597*, 230−234.
(3) Kong, X. Y.; Tan, W. L.; Ng, B.-J; Chai, S.-P; Mohamed, A. R. Harnessing Vis−NIR Broad Spectrum for Photocatalytic $CO_2$ Reduction over Carbon Quantum Dots-Decorated Ultrathin $Bi_2WO_6$ Nanosheets. *Nano Res.* **2017**, *10*, 1720−1731.
(4) Roger, I.; Shipman, M. A.; Symes, M. D. Earth-Abundant Catalysts for Electrochemical and Photoelectrochemical Water Splitting. *Nat. Rev. Chem.* **2017**, *1*, 3.
(5) Zhu, J.; Hu, L.; Zhao, P.; Lee, L. Y. S.; Wong, K.-Y. Recent Advances in Electrocatalytic Hydrogen Evolution using Nanoparticles. *Chem. Rev.* **2020**, *120*, 851−918.
(6) Jiao, F.; Xu, B. Electrochemical Ammonia Synthesis and Ammonia Fuel Cells. *Adv. Mater.* **2019**, *31*, 1805173.
(7) Feng, X.; Zou, H.; Zheng, R.; Wei, W.; Wang, R.; Zou, W.; Lim, G.; Hong, J.; Duan, L.; Chen, H. $Bi_2O_3$/$BiO_2$ Nanoheterojunction for Highly Efficient Electrocatalytic $CO_2$ Reduction to Formate. *Nano Lett.* **2022**, *22*, 1656−1664.
(8) Sim, Y.; Chae, Y.; Kwon, S.-Y. Recent advances in Metallic Transition Metal Dichalcogenides as Electrocatalysts for Hydrogen Evolution Reaction. *iScience* **2022**, *25*, 105098.
(9) Li, B.; Wang, W.; Zhao, J.; Wang, Z.; Su, B.; Hou, Y.; Ding, Z.; Ong, W.-J.; Wang, S. All-Solid-State Direct Z-Scheme $NiTiO_3$/$Cd_{0.5}Zn_{0.5}S$ Heterostructures for Photocatalytic Hydrogen Evolution with Visible Light. *J. Mater. Chem. A* **2021**, *9*, 10270−10276.
(10) Wu, L.; Zhang, F.; Song, S.; Ning, M.; Zhu, Q.; Zhou, J.; Gao, G.; Chen, Z.; Zhou, Q.; Xing, X.; Tong, T.; Yao, Y.; Bao, J.; Yu, L.; Chen, S.; Ren, Z. Efficient Alkaline Water/Seawater Hydrogen Evolution by a Nanorod-Nanoparticle-Structured Ni-MoN Catalyst with Fast Water-Dissociation Kinetics. *Adv. Mater.* **2022**, *34*, 2201774.

(11) Lu, X. F.; Zhang, S. L.; Sim, W. L.; Gao, S.; Lou, X. W. Phosphorized CoNi$_2$S$_4$ Yolk-Shell Spheres for Highly Efficient Hydrogen Production via Water and Urea Electrolysis. *Angew. Chem., Int. Ed.* **2021**, *60*, 22885−22891.

(12) Chen, Y.; Qiao, Q.; Cao, J.; Li, H.; Bian, Z. Precious Metal Recovery. *Joule* **2021**, *5*, 3097−3115.

(13) Wang, S.; Wang, Y.; Zhang, S. L.; Zang, S.-Q.; Lou, X. W. Supporting Ultrathin ZnIn$_2$S$_4$ Nanosheets on Co/N-Doped Graphitic Carbon Nanocages for Efficient Photocatalytic H$_2$ Generation. *Adv. Mater.* **2019**, *31*, 1903404.

(14) Glaister, B. J.; Mudd, G. M. The Environmental Costs of Platinum−PGM Mining and Sustainability: Is the Glass Half-Full or Half-Empty? *Miner. Eng.* **2010**, *23*, 438−450.

(15) Xiong, Z.; Hou, Y.; Yuan, R.; Ding, Z.; Ong, W.-J.; Wang, S. Hollow NiCo$_2$S$_4$ Nanospheres as a Cocatalyst to Support ZnIn$_2$S$_4$ Nanosheets for Visible-Light-Driven Hydrogen Production. *Acta Physico-Chimica Sin.* **2022**, *38*, 2111021.

(16) Chhowalla, M.; Shin, H. S.; Eda, G.; Li, L.-J.; Loh, K. P.; Zhang, H. The Chemistry of Two-Dimensional Layered Transition Metal Dichalcogenide Nanosheets. *Nat. Chem.* **2013**, *5*, 263−275.

(17) Hinnemann, B.; Moses, P. G.; Bonde, J.; Jørgensen, K. P.; Nielsen, J. H.; Horch, S.; Chorkendorff, I.; Nørskov, J. K. Biomimetic Hydrogen Evolution: MoS$_2$ Nanoparticles as Catalyst for Hydrogen Evolution. *J. Am. Chem. Soc.* **2005**, *127*, 5308−5309.

(18) Xu, Y.; Zheng, C.; Wang, S.; Hou, Y. 3D Arrays of Molybdenum Sulphide Nanosheets on Mo Meshes: Efficient Electrocatalysts for Hydrogen Evolution Reaction. *Electrochim. Acta* **2015**, *174*, 653−659.

(19) Wu, X.; Zhang, H.; Zhang, J.; Lou, X. W. D. Recent Advances on Transition Metal Dichalcogenides for Electrochemical Energy Conversion. *Adv. Mater.* **2021**, *33*, 2008376.

(20) Benck, J. D.; Hellstern, T. R.; Kibsgaard, J.; Chakthranont, P.; Jaramillo, T. F. Catalyzing the Hydrogen Evolution Reaction (HER) with Molybdenum Sulfide Nanomaterials. *ACS Catal.* **2014**, *4*, 3957−3971.

(21) Kong, D.; Wang, H.; Cha, J. J.; Pasta, M.; Koski, K. J.; Yao, J.; Cui, Y. Synthesis of MoS$_2$ and MoSe$_2$ Films with Vertically Aligned Layers. *Nano Lett.* **2013**, *13*, 1341−1347.

(22) Voiry, D.; Salehi, M.; Silva, R.; Fujita, T.; Chen, M.; Asefa, T.; Shenoy, V. B.; Eda, G.; Chhowalla, M. Conducting MoS$_2$ Nanosheets as Catalysts for Hydrogen Evolution Reaction. *Nano Lett.* **2013**, *13*, 6222−6227.

(23) Parsons, R. The Rate of Electrolytic Hydrogen Evolution and the Heat of Adsorption of Hydrogen. *Trans. Faraday Soc.* **1958**, *54*, 1053−1063.

(24) McCrory, C. C. L.; Jung, S.; Ferrer, I. M.; Chatman, S. M.; Peters, J. C.; Jaramillo, T. F. Benchmarking Hydrogen Evolving Reaction and Oxygen Evolving Reaction Electrocatalysts for Solar Water Splitting Devices. *J. Am. Chem. Soc.* **2015**, *137*, 4347−4357.

(25) Wei, C.; Rao, R. R.; Peng, J.; Huang, B.; Stephens, I. E. L.; Risch, M.; Xu, Z. J.; Shao-Horn, Y. Recommended Practices and Benchmark Activity for Hydrogen and Oxygen Electrocatalysis in Water Splitting and Fuel Cells. *Adv. Mater.* **2019**, *31*, 1806296.

(26) Wang, C.; Shang, H.; Jin, L.; Xu, H.; Du, Y. Advances in Hydrogen Production from Electrocatalytic Seawater Splitting. *Nanoscale* **2021**, *13*, 7897−7912.

(27) Prats, H.; Chan, K. The Determination of the HOR/HER Reaction Mechanism from Experimental Kinetic Data. *Phys. Chem. Chem. Phys.* **2021**, *23*, 27150−27158.

(28) Boudart, M. *Kinetics of Chemical Processes*; Prentice-Hall, Inc.: Englewood Cliffs, 1968.

(29) Boudart, M. Turnover Rates in Heterogeneous Catalysis. *Chem. Rev.* **1995**, *95*, 661−666.

(30) Kong, X. Y.; Choo, Y. Y.; Chai, S.-P.; Soh, A. K.; Mohamed, A. R. Oxygen Vacancy Induced Bi2WO6 for the Realization of Photocatalytic CO$_2$ Reduction over the Full Solar Spectrum: From the UV to the NIR Region. *Chem. Commun.* **2016**, *52*, 14242−14245.

(31) Kobayashi, S.; Mizumukai, Y.; Ohnishi, T.; Shibata, N.; Ikuhara, Y.; Yamamoto, T. High Electron Mobility of Nb-Doped SrTiO$_3$ Films

Stemming from Rod-Type Sr Vacancy Clusters. *ACS Nano* **2015**, *9*, 10769−10777.

(32) Yang, C.; Lu, Y.; Zhang, L.; Kong, Z.; Yang, T.; Tao, L.; Zou, Y.; Wang, S. Defect Engineering on CeO$_2$-Based Catalysts for Heterogeneous Catalytic Applications. *Small Struct.* **2021**, *2*, 2100058.

(33) Kong, X. Y.; Ng, B.-J.; Tan, K. H.; Chen, X.; Wang, H.; Mohamed, A. R.; Chai, S.-P. Simultaneous Generation of Oxygen Vacancies on Ultrathin BiOBr Nanosheets during Visible-Light-Driven CO$_2$ Photoreduction Evoked Superior Activity and Long-Term Stability. *Catal. Today* **2018**, *314*, 20−27.

(34) Kong, X. Y.; Lee, W. P. C.; Ong, W.-J.; Chai, S.-P.; Mohamed, A. R. Oxygen-Deficient BiOBr as a Highly Stable Photocatalyst for Efficient CO$_2$ Reduction into Renewable Carbon-Neutral Fuels. *ChemCatChem* **2016**, *8*, 3074−3081.

(35) Cao, Y. Roadmap and Direction toward High-Performance MoS$_2$ Hydrogen Evolution Catalysts. *ACS Nano* **2021**, *15*, 11014−11039.

(36) Yan, Y.; Xia, B.; Xu, Z.; Wang, X. Recent Development of Molybdenum Sulfides as Advanced Electrocatalysts for Hydrogen Evolution Reaction. *ACS Catal.* **2014**, *4*, 1693−1705.

(37) Kibsgaard, J.; Chen, Z.; Reinecke, B. N.; Jaramillo, T. F. Engineering the Surface Structure of MoS$_2$ to Preferentially Expose Active Edge Sites for Electrocatalysis. *Nat. Mater.* **2012**, *11*, 963−969.

(38) Li, Y.; Zuo, S.; Li, Q.-H.; Wu, X.; Zhang, J.; Zhang, H.; Zhang, J. Vertically Aligned MoS$_2$ with In-Plane Selectively Cleaved Mo−S Bond for Hydrogen Production. *Nano Lett.* **2021**, *21*, 1848−1855.

(39) Jiao, Y.; Hafez, A. M.; Cao, D.; Mukhopadhyay, A.; Ma, Y.; Zhu, H. Metallic MoS$_2$ for High Performance Energy Storage and Energy Conversion. *Small* **2018**, *14*, 1800640.

(40) Lukowski, M. A.; Daniel, A. S.; Meng, F.; Forticaux, A.; Li, L.; Jin, S. Enhanced Hydrogen Evolution Catalysis from Chemically Exfoliated Metallic MoS$_2$ Nanosheets. *J. Am. Chem. Soc.* **2013**, *135*, 10274−10277.

(41) Xie, C.; Yan, D.; Li, H.; Du, S.; Chen, W.; Wang, Y.; Zou, Y.; Chen, R.; Wang, S. Defect Chemistry in Heterogeneous Catalysis: Recognition, Understanding, and Utilization. *ACS Catal.* **2020**, *10*, 11082−11098.

(42) Yin, Y.; Han, J.; Zhang, Y.; Zhang, X.; Xu, P.; Yuan, Q.; Samad, L.; Wang, X.; Wang, Y.; Zhang, Z.; Zhang, P.; Cao, X.; Song, B.; Jin, S. Contributions of Phase, Sulfur Vacancies, and Edges to the Hydrogen Evolution Reaction Catalytic Activity of Porous Molybdenum Disulfide Nanosheets. *J. Am. Chem. Soc.* **2016**, *138*, 7965−7972.

(43) Liu, Y.; Xiao, C.; Li, Z.; Xie, Y. Vacancy Engineering for Tuning Electron and Phonon Structures of Two-Dimensional Materials. *Adv. Energy Mater.* **2016**, *6*, 1600436.

(44) Zhu, J.; Wang, Z.-C.; Dai, H.; Wang, Q.; Yang, R.; Yu, H.; Liao, M.; Zhang, J.; Chen, W.; Wei, Z.; Li, N.; Du, L.; Shi, D.; Wang, W.; Zhang, L.; Jiang, Y.; Zhang, G. Boundary Activated Hydrogen Evolution Reaction on Monolayer MoS$_2$. *Nat. Commun.* **2019**, *10*, 1348.

(45) Yang, J.; Wang, Y.; Lagos, M. J.; Manichev, V.; Fullon, R.; Song, X.; Voiry, D.; Chakraborty, S.; Zhang, W.; Batson, P. E.; Feldman, L.; Gustafsson, T.; Chhowalla, M. Single Atomic Vacancy Catalysis. *ACS Nano* **2019**, *13*, 9958−9964.

(46) Wang, X.; Zhang, Y.; Si, H.; Zhang, Q.; Wu, J.; Gao, L.; Wei, X.; Sun, Y.; Liao, Q.; Zhang, Z.; Ammarah, K.; Gu, L.; Kang, Z.; Zhang, Y. Single-Atom Vacancy Defect to Trigger High-Efficiency Hydrogen Evolution of MoS$_2$. *J. Am. Chem. Soc.* **2020**, *142*, 4298−4308.

(47) Jiao, S.; Yao, Z.; Xue, F.; Lu, Y.; Liu, M.; Deng, H.; Ma, X.; Liu, Z.; Ma, C.; Huang, H.; Ruan, S.; Zeng, Y.-J. Defect-Rich One-Dimensional MoS$_2$ Hierarchical Architecture for Efficient Hydrogen Evolution: Coupling of Multiple Advantages into One Catalyst. *Appl. Catal., B* **2019**, *258*, 117964.

(48) Jiang, L.; Zhou, Q.; Li, J.-J.; Xia, Y.-X.; Li, H.-X.; Li, Y.-J. Engineering Isolated S Vacancies over 2D MoS$_2$ Basal Planes for Catalytic Hydrogen Evolution. *ACS Appl. Nano Mater.* **2022**, *5*, 3521−3530.

(49) Wu, W.; Niu, C.; Wei, C.; Jia, Y.; Li, C.; Xu, Q. Activation of $MoS_2$ Basal Planes for Hydrogen Evolution by Zinc. *Angew. Chemie Int. Ed.* **2019**, *58*, 2029−2033.

(50) Li, L.; Qin, Z.; Ries, L.; Hong, S.; Michel, T.; Yang, J.; Salameh, C.; Bechelany, M.; Miele, P.; Kaplan, D.; Chhowalla, M.; Voiry, D. Role of Sulfur Vacancies and Undercoordinated Mo Regions in $MoS_2$ Nanosheets toward the Evolution of Hydrogen. *ACS Nano* **2019**, *13*, 6824−6834.

(51) Xu, J.; Shao, G.; Tang, X.; Lv, F.; Xiang, H.; Jing, C.; Liu, S.; Dai, S.; Li, Y.; Luo, J.; Zhou, Z. Frenkel-Defected Monolayer $MoS_2$ Catalysts for Efficient Hydrogen Evolution. *Nat. Commun.* **2022**, *13*, 2193.

(52) Li, S.; Zhou, S.; Wang, X.; Tang, P.; Pasta, M.; Warner, J. H. Increasing the Electrochemical Activity of Basal Plane Sites in Porous 3D Edge Rich $MoS_2$ Thin Films for the Hydrogen Evolution Reaction. *Mater. Today Energy* **2019**, *13*, 134−144.

(53) Kuraganti, V.; Jain, A.; Bar-Ziv, R.; Ramasubramaniam, A.; Bar-Sadan, M. Manganese Doping of $MoSe_2$ Promotes Active Defect Sites for Hydrogen Evolution. *ACS Appl. Mater. Interfaces* **2019**, *11*, 25155−25162.

(54) Kwon, I. S.; Kwak, I. H.; Kim, J. Y.; Debela, T. T.; Park, Y. C.; Park, J.; Kang, H. S. Concurrent Vacancy and Adatom Defects of $Mo_{1−x}Nb_xSe_2$ Alloy Nanosheets Enhance Electrochemical Performance of Hydrogen Evolution Reaction. *ACS Nano* **2021**, *15*, 5467−5477.

(55) Kwon, I. S.; Kwak, I. H.; Debela, T. T.; Kim, J. Y.; Yoo, S. J.; Kim, J.-G.; Park, J.; Kang, H. S. Phase-Transition $Mo_{1−x}V_xSe_2$ Alloy Nanosheets with Rich V−Se Vacancies and Their Enhanced Catalytic Performance of Hydrogen Evolution Reaction. *ACS Nano* **2021**, *15*, 14672−14682.

(56) Xia, X.; Zhao, G.; Yan, Q.; Wang, B.; Wang, Q.; Xie, H. High-Density Defects Activating Fe-Doped Molybdenum Sulfide@N-Doped Carbon Heterostructures for Efficient Electrochemical Hydrogen Evolution. *ACS Sustain. Chem. Eng.* **2022**, *10*, 182−193.

(57) Tang, J.; Chu, Y.; Wang, K.; Deng, B.; Li, Y.; Tan, X. Facile In Situ Synthesis of an Ultrafine and Defect-Rich Co-Doped $MoS_2$ Nanocluster Catalyst for Efficient Hydrogen Evolution Reaction in Alkaline Medium. *ACS Appl. Energy Mater.* **2021**, *4*, 2300−2306.

(58) Zhao, R.; Deng, K.; Tian, W.; Hu, Z.; Lv, X.; Ma, K.; Peng, W.; Ji, J. P-Doped $MoSe_2/MoS_2$ Heterojunctions Anchored on N-CNTs/ Carbon Cloth with Abundant Interfaces and Defects for Effective Electrocatalytic Hydrogen Evolution. *ACS Appl. Energy Mater.* **2021**, *4*, 2408−2418.

(59) Chua, X. J.; Luxa, J.; Eng, A. Y. S.; Tan, S. M.; Sofer, Z.; Pumera, M. Negative Electrocatalytic Effects of P-Doping Niobium and Tantalum on $MoS_2$ and $WS_2$ for the Hydrogen Evolution Reaction and Oxygen Reduction Reaction. *ACS Catal.* **2016**, *6*, 5724−5734.

(60) Sun, J.; Huang, Z.; Huang, T.; Wang, X.; Wang, X.; Yu, P.; Zong, C.; Dai, F.; Sun, D. Defect-Rich Porous $CoS_{1.097}/MoS_2$ Hybrid Microspheres as Electrocatalysts for pH-Universal Hydrogen Evolution. *ACS Appl. Energy Mater.* **2019**, *2*, 7504−7511.

(61) He, Z.; Liu, Q.; Zhu, Y.; Tan, T.; Cao, L.; Zhao, S.; Chen, Y. Defect-Mediated Adsorption of Metal Ions for Constructing Ni Hydroxide/$MoS_2$ Heterostructures as High-Performance Water-Splitting Electrocatalysts. *ACS Appl. Energy Mater.* **2020**, *3*, 7039−7047.

(62) Duraisamy, S.; Ganguly, A.; Sharma, P. K.; Benson, J.; Davis, J.; Papakonstantinou, P. One-Step Hydrothermal Synthesis of Phase-Engineered $MoS_2/MoO_3$ Electrocatalysts for Hydrogen Evolution Reaction. *ACS Appl. Nano Mater.* **2021**, *4*, 2642−2656.

(63) Xu, Y.; Fo, Y.; Lv, H.; Cui, X.; Liu, G.; Zhou, X.; Jiang, L. Anderson-Type Polyoxometalate-Assisted Synthesis of Defect-Rich Doped 1T/2H-$MoSe_2$ Nanosheets for Efficient Seawater Splitting and Mg/Seawater Batteries. *ACS Appl. Mater. Interfaces* **2022**, *14*, 10246−10256.

(64) Chen, L.; Feng, H.; Zhang, R.; Wang, S.; Zhang, X.; Wei, Z.; Zhu, Y.; Gu, M.; Zhao, C. Phase-Controlled Synthesis of 2H/3R-$MoSe_2$ Nanosheets on P-Doped Carbon for Synergistic Hydrogen Evolution. *ACS Appl. Nano Mater.* **2020**, *3*, 6516−6523.

(65) Cui, Y.; Guo, X.; Zhang, J.; Li, X.; Zhu, X.; Huang, W. Di-Defects Synergy Boost Electrocatalysis Hydrogen Evolution over Two-Dimensional Heterojunctions. *Nano Res.* **2022**, *15*, 677−684.

(66) Sarma, P. V.; Kayal, A.; Sharma, C. H.; Thalakulam, M.; Mitra, J.; Shaijumon, M. M. Electrocatalysis on Edge-Rich Spiral $WS_2$ for Hydrogen Evolution. *ACS Nano* **2019**, *13*, 10448−10455.

(67) Sun, J.; Hu, X.; Huang, Z.; Huang, T.; Wang, X.; Guo, H.; Dai, F.; Sun, D. Atomically Thin Defect-Rich Ni-Se-S Hybrid Nanosheets as Hydrogen Evolution Reaction Electrocatalysts. *Nano Res.* **2020**, *13*, 2056−2062.

(68) Huang, S.; Jin, Z.; Ning, P.; Gao, C.; Wu, Y.; Liu, X.; Xin, P.; Chen, Z.; Jiang, Y.; Hu, Z.; Chen, Z. Synergistically Modulating Electronic Structure of $NiS_2$ Hierarchical Architectures by Phosphorus Doping and Sulfur-Vacancies Defect Engineering Enables Efficient Electrocatalytic Water Splitting. *Chem. Eng. J.* **2021**, *420*, 127630.